Thermospheric Composition and Solar EUV Flux from the Global-scale Observations of the Limb and Disk (GOLD) mission

John Correira[1,1], Joseph S. Evans[2,2], Andrey Kyrwonos[3,3], Jerry D. Lumpe[4,4], Victoir Veibell[5,5], William E. McClintock[6,6], and Richard Eastes[6,6]

[1]Computational Physics, Inc.
[2]Computational Physics, Incorporated
[3]Florida Space Institute, University of Central Florida
[4]Computational Physics Inc.
[5]Computational Physics Inc
[6]Laboratory for Atmospheric and Space Physics

November 30, 2022

Abstract

Observations of far-ultraviolet (FUV) dayglow by the Global-scale Observations of Limb and Disk (GOLD) mission provide a new opportunity to monitor relative composition changes in the upper atmosphere as well as solar extreme ultraviolet (EUV) variability. Relative composition changes are quantified by ΣO/N2, the column density ratio of atomic oxygen to molecular nitrogen, while QEUV provides a measure of the solar EUV energy flux from 1 to 45 nm into the upper atmosphere. This spectral range provides the ionizing radiation which ultimately results in FUV airglow emission produced by photodissociation and photoelectron impact. The quantities ΣO/N2 and QEUV are derived from GOLD FUV observations through lookup tables that are constructed using a first-principles photoelectron transport model. The two FUV emissions used are O I 135.6 nm and the N2 Lyman-Birge-Hopfield (LBH) bands. We present an overview of the theoretical basis for the algorithms and practical considerations for application to GOLD data. The effects of uncertainties in electron impact cross sections, off-nadir viewing, and instrument artifacts are reviewed. We also discuss GOLD Level 1C DAY, Level 2 data products ON2 and QEUV, and present representative samples of each.

Thermospheric Composition and Solar EUV Flux from the Global-scale Observations of the Limb and Disk (GOLD) mission

J. Correira[1], J. D. Lumpe[2], J. S. Evans[1], A. Krywonos[3], R. Daniell[4], V. Veibell[1], W. E. McClintock[5], and R. W. Eastes[5]

[1]Computational Physics, Inc., Springfield, Virginia, USA
[2]Computational Physics, Inc., Boulder, CO, USA
[3]Florida Space Institute, University of Central Florida, Orlando, Florida, USA
[4]Ionospheric Physics Consulting, Stoughton, MA, USA
[5]Laboratory for Atmospheric and Space Physics, University of Colorado, Boulder, Colorado, USA

Key Points:

- GOLD's vantage point from geostationary orbit provides a large scale, high cadence, synoptic view for more than 18 hours each day.
- The evolution of a geomagnetic storm shows a ON2 depletion of over 40% at high latitudes and a corresponding enhancement at low latitudes.
- Despite historically low solar activity during the first two years of the GOLD mission, mean derived QEUV values correlate well with F10.7.

Corresponding author: John Correira, correira@cpi.com

Abstract

Observations of far-ultraviolet (FUV) dayglow by the Global-scale Observations of Limb and Disk (GOLD) mission provide a new opportunity to monitor relative composition changes in the upper atmosphere as well as solar extreme ultraviolet (EUV) variability. Relative composition changes are quantified by $\Sigma O/N_2$, the column density ratio of atomic oxygen to molecular nitrogen, while Q_{EUV} provides a measure of the solar EUV energy flux from 1 to 45 nm into the upper atmosphere. This spectral range provides the ionizing radiation which ultimately results in FUV airglow emission produced by photodissociation and photoelectron impact. The quantities $\Sigma O/N_2$ and Q_{EUV} are derived from GOLD FUV observations through lookup tables that are constructed using a first-principles photoelectron transport model. The two FUV emissions used are O I 135.6 nm and the N_2 Lyman-Birge-Hopfield (LBH) bands. We present an overview of the theoretical basis for the algorithms and practical considerations for application to GOLD data. The effects of uncertainties in electron impact cross sections, off-nadir viewing, and instrument artifacts are reviewed. We also discuss GOLD Level 1C DAY, Level 2 data products ON2 and QEUV, and present representative samples of each.

1 Introduction

Global-scale Observations of the Limb and Disk (GOLD) is a PI-led NASA mission of opportunity that was launched on 25 January 2018 as a hosted payload on the SES-14 commercial communications satellite. GOLD science operations began in October 2018. The primary objective of GOLD is to answer fundamental scientific questions about how the Earth's thermosphere-ionosphere system responds to geomagnetic storms, solar radiation, and upward propagating tides. To help answer these questions, GOLD utilizes two identical but independent imaging spectrographs. From its vantage point in geostationary orbit at 47.5° W longitude GOLD images the Earth in the far-ultraviolet (FUV). GOLD observes the disk of the Earth for 18.5 hours per day while also performing routine limb scan and stellar occultation measurements. GOLD science algorithms use the observed spectra to produce Level 2 data products that include: daytime neutral temperatures near the peak of the N_2 LBH emitting layer (Level 2 data product TDISK); daytime and nighttime thermospheric molecular oxygen density profiles (O2DEN); daytime exospheric neutral temperature on the limb (TLIMB); daytime ratios of atomic

oxygen and molecular nitrogen column densities (ON2); and integrated solar EUV energy flux between 1 and 45 nm (QEUV).

The ON2 and QEUV data products are pertinent to several aspects of the GOLD science objectives. Changes in $\Sigma O/N_2$ are of particular interest. Analyses of DE-1 FUV imaging data (Craven et al., 1994; Nicholas et al., 1997; Immel et al., 1997, 2001; Drob et al., 1999; Strickland, Cox, et al., 1999; Strickland et al., 2001; Strickland, 2001) and TIMED/GUVI data (Strickland, Lean, et al., 2004; Meier et al., 2005; Crowley et al., 2006; Strickland et al., 2007; Crowley et al., 2008) have shown significant variation in both magnitude (depletions of more than a factor of two) and spatial extent of the response to high latitude heating and dynamics. Typical quiet-time seasonal variations of a factor of two or more between solstices have been reported (Strickland, Meier, et al., 2004). Early examinations of GOLD dayglow data show that important new insights into composition disturbances and associated dynamics will be gained from analysis of such data (Oberheide et al., 2020; Aryal et al., 2020; Cai et al., 2020). Q_{EUV} provides a measure of solar EUV that can be related to direct solar measurements, such as those made by the SEE instrument (Woods et al., 1998). Q_{EUV} has been used for validation of XUV Photometer System spectra (Woods et al., 2008) and to study solar flares (Strickland et al., 2007).

In this technical report we describe the GOLD Level 2 science data products ON2 and QEUV. Section 2 provides further details on the GOLD instrument and observations relevant to deriving $\Sigma O/N_2$ and discusses the FUV dayglow features observed by GOLD. As the algorithm used for generating GOLD Level 2 ON2 data products relies upon the well established work of Strickland et al. (1995), Section 3 briefly reviews the essential points, discusses common misconceptions regarding the meaning and interpretation of $\Sigma O/N_2$ derived from remotely sensed dayglow data, provides details about specific application to GOLD disk observations, and discusses the lookup tables that drive the algorithms. In a similar fashion, Section 4 presents details of the Q_{EUV} algorithm and Level 2 data product.

2 The GOLD Instrument

The GOLD instrument is a dual channel UV spectrograph, which images the Earth's airglow from ∼134 to 162 nm (Eastes et al., 2017). The two channels are identical and

can be operated independently, allowing either channel to be used for any of GOLD's operating modes. Each channel consists of a scan mirror mechanism located in front of a spherical telescope mirror, which images the Earth onto a spectrograph entrance slit. The combination of a concave toroidal mirror and concave toroidal grating is then used to disperse the input beam and re-image the entrance slit onto a microchannel plate (MCP) detector, forming a two dimensional spectral-spatial image of the slit. Each channel can use one of three interchangeable slits - high resolution (HR, 0.2 mm), low resolution (LR, 0.4 mm), and occultation (OCC - 2.6 mm). The HR slit is used when scanning the limb. The HR slit is also typically used for disk scans. The OCC slit is only used when performing stellar occultations. The scan mirror mechanism consists of back-to-back, tilted plane mirrors, allowing each channel to scan either the northern or southern hemisphere. When the scan mirror's field-of-view is swept across the Earth, at each scan mirror position the detector records the x-y locations of individual photons as they arrive at the detector. No data processing is done on the spacecraft. The photon positions and times are sent directly to the ground where they are binned to produce spatial-spectral image cubes. This allows greater flexibility in determining the binning to use for GOLD's data products and is enabled by the continuous, high data rate downlink provided by the host spacecraft. The foregoing details have been largely confined to those relevant to the $\Sigma O/N_2$ and Q_{EUV} algorithms. Readers interested in learning more about the GOLD instrument, as well as descriptions of GOLD's mission operations and other observing modes, may refer to Eastes et al. (2020) and McClintock et al. (2020).

GOLD observes the Earth 18.5 hours per day from 06:10 UT to 00:40 UT. During the remaining time, when the Sun is within 30° of the instrument's field of regard, GOLD is placed in Solar Safe mode. GOLD's routine observations consist of four different observation scenarios: dayside disk scans; limb scans (Evans et al., 2020); occultations (Lumpe et al., 2020); and nightside disk scans (Eastes et al., 2019). DAY disk scans begin at 03:00 satellite local time (06:10 UT) and occur on a 30-minute cadence. The northern and southern hemispheres are scanned separately from east to west with each scan lasting 12 minutes. Two consecutive scans cover the entire disk of the Earth visible from GOLD, including both the sunlit and nighttime portions. Two limb scans (north and south hemisphere) take place at the end of every disk scan sequence, unless an occultation occurs during that half hour segment.

The dominant spectral features present in the UV spectra measured by GOLD are:

1. O I doublet at 135.56 nm and 135.85 nm from the $^5S^\circ \rightarrow {}^3P$ transition.
2. N I doublet at 149.26 nm and 149.28 nm from the $^2P \rightarrow {}^2D^\circ$ transition.
3. Lyman-Birge-Hopfield (LBH) band system of molecular nitrogen arising from the a $\rightarrow$ X state transition.

Early in the mission the O I singlet at 164.13 nm from the forbidden $^3S^\circ \rightarrow {}^1D$ transition was imaged on the detector but subsequent shifts to the wavelengths observed have moved this emission line off the active part of the detector.

In the upper atmosphere the dominant mechanism for excitation to the upper state for both the O I 135.6 nm and N_2 LBH emissions is inelastic collisions with electrons: $X + e^- \rightarrow X^* + e^-$. These electrons are initially produced by ionization of atmospheric species by solar photons. The 149.3 nm emission is produced by electron impact on N, electron impact dissociative excitation of N_2 ($N_2 + e^- \rightarrow N^* + N + e^-$), and photodissociative ionization excitation ($N_2 + h\nu \rightarrow N^* + N^+ + e^-$) and photodissociative excitation ($N_2 + h\nu \rightarrow N^* + N$) of N_2 (Bishop & Feldman, 2003). If the contribution from electron impact on N is relatively small then 149.3 nm emission could be combined with LBH as a signature of N_2. However, there remains some uncertainty as to the relative contributions of N and N_2 to the 149.3 nm emission (Meier et al., 1991; Zhang et al., 2018). The 164.1 nm emission is produced primarily by electron impact on O (there is a weak contribution from electron impact on O_2) and this emission is an alternative decay path from the ^3S state, which also produces the optically thick 130.4 nm emission feature. In light of uncertainties associated with the 149.3 nm and 164.1 nm emission features, they are not used in the $\Sigma O/N_2$ or Q_{EUV} algorithms and will not be discussed further.

The emission features discussed can be seen in the GOLD spectrum shown in the upper panel of Figure 1. The spectrum shown is a combination of 4 L1C spectra, representative of what is used by the Level 2 ON2 algorithm (see Section 3.3). The three atomic emission features and prominent LBH bands are identified. In cases where multiple LBH bands overlap the brighter band is identified. Also note that the (3,0) LBH band at 135.4 nm is not identified due to overlap with O I 135.6 nm. The lower panel of Figure 1 shows a 135.6 nm intensity from two consecutive DAY scans starting at 15:10 and 15:22 UT on 3 November 2018 (day of year 307). Here the definition of 135.6 nm intensity is the same as used with the lookup tables (see Section 3.3). The effect of bright-

ening from increased path length can be seen near the edges of the disk and an airglow layer on the limb is clearly evident.

3 $\Sigma O/N_2$

3.1 Algorithm

The intensity ratio of 135.6 nm to LBH as observed by GOLD during disk scans can be used to derive the column density ratio $\Sigma O/N_2$. The concept was introduced and discussed by Strickland et al. (1995) but using different definitions of 135.6 nm and LBH. As noted in Strickland et al. (1995): "Analysis of data from a different instrument having a different wavelength resolution requires a recalculation of these results for that resolution and over wavelength intervals that will likely be different ...".

The crux of the $\Sigma O/N_2$ algorithm lies in the correspondence between the equations giving the ratio of integrated emissions and column densities, namely

$$\frac{I_{135.6}}{I_{LBH}} = \frac{\int_{N_{T0}}^{0} f_O(N_T) g_{135.6}(N_T)\, dN_T}{\int_{N_{T0}}^{0} f_{N_2}(N_T) g_{\mathrm{LBH}}(N_T)\, dN_T} \tag{1}$$

and

$$\Sigma O/N_2 = \frac{N_O}{N_{N_2}} = \frac{\int f_O(N_T) dN_T}{\int f_{N_2}(N_T) dN_T} \tag{2}$$

where

I_b is the measured intensity ($b = \{135.6, LBH\}$)

f_s is the mixing ratio ($s = \{O, N_2\}$)

N is the number density, either of O or N_2, or the total number density when used with the T subscript.

g_s is the g-factor (photons s^{-1})

Equations 1 and 2 differ only by the presence of the g-factors in Equation 1, which act as weighting factors on the mixing ratios (i.e. Equation 1 is essentially a weighted version of Equation 2). The relationship between the column density ratio and intensity ratio can be determined by modeling and stored in lookup tables.

A necessary condition for deriving $\Sigma O/N_2$ from observed intensity ratios is that for a given atmosphere the intensity ratio is essentially constant as the solar EUV spectrum varies. Strickland et al. (1995) observed an approximately constant ratio for their selected wavelength intervals using the Hinteregger spectrum (Hinteregger et al., 1981).

This enables one to unambiguously attribute observed changes in 135.6 nm/LBH to changes in the atmosphere rather than variations in the solar input.

The lower limit of integration should be large enough to encompass the region where most of the emissions of interest originate from but not so large that most of the column comes from below the region of emission. Strickland et al. (1995) demonstrate that for $\Sigma O/N_2$ derived from the 135.6 nm/LBH intensity ratio a value of $N = 10^{17}\text{cm}^{-2}$ for N_2 minimizes the uncertainty in the relationship between intensity and column density ratio (i.e. it maximizes the uniqueness between the two). The significance of the value of 10^{17}cm^{-2} is discussed further in Section 3.2.2.

A longer derivation is provided in the Supporting Information, while Strickland et al. (1995) provides a more detailed discussion of the algorithm. Strickland et al. (1993) also contains valuable qualitative insights into the physical meaning of $\Sigma O/N_2$.

3.2 Lookup Tables

Lookup tables are constructed by first selecting a reference atmosphere and constructing a two-dimensional grid in O density scaling factors (f_O) and solar zenith angle (SZA). In this case, an NRLMSISE-00 atmosphere (Picone et al., 2002) was used, but as discussed in Strickland et al. (1995), the choice of reference atmosphere has an insignificant effect on the tables (assuming a physically realistic atmosphere). The f_O scaling factors applied to the model atmosphere range from 0.2 to 3.0 with a step size of 0.01, corresponding to a range of $\Sigma O/N_2$ values of $\sim$0.016 to $\sim$2.5. For each of these f_O scale factors, a SZA grid of 0° to 88° with a 2° step size is constructed. Except during solar flare conditions, the choice of solar spectrum has a weak effect on the lookup tables since the 135.6 nm/LBH intensity ratio remains effectively unchanged. For the GOLD tables a solar spectrum is constructed from the NRLEUV model scaled by SEE data (Warren, 2005), taking the average of 231 spectra with a F10.7 value between 62.5 and 67.5 (s.f.u.). During a solar flare the increase in photon energy at shorter wavelengths requires the use of flare specific lookup tables for derivation of accurate $\Sigma O/N_2$ (Strickland et al., 2007). At the current time no attempt is made to correct GOLD data for flare conditions, though flare specific lookup tables will be considered for a future version.

The AURIC model (Strickland, Bishop, et al., 1999) is used to calculate column emission rates and spectral radiances as functions of both $\Sigma O/N_2$ and SZA for the range

of inputs described above. The model uses a multistream transport solution to the electron transport equation. Multiple scattering effects are included in the column emission rates for electron impact on O through the REDISTER model (Gladstone, 1982, 1988) within AURIC. Single scattering is assumed for electron impact on O_2 due to the assumption that significant emission from the O fragments is Doppler shifted outside of the core of the absorption line profile.

Electron impact cross sections are an important consideration when modeling airglow and constructing the lookup tables. Errors in adopted cross sections, and more specifically relative errors between the 135.6 nm and LBH cross sections, can create a bias in derived $\Sigma O/N_2$. While an absolute bias in $\Sigma O/N_2$ is unavoidable due to cross section errors, relative variations in $\Sigma O/N_2$ derived from GOLD data are essentially unaffected by such systematic offsets. The notable electron impact cross sections used are: Meier (1991) for the production of O I 135.6 nm from atomic oxygen; Kanik et al. (2003) for O I 135.6 nm from molecular oxygen; and Ajello and Shemansky (1985) for the production of LBH from molecular nitrogen. The Ajello and Shemansky (1985) cross section is scaled by a factor of 1.351 to account for a combination of radiative and collisional cascading (Eastes, 2000), emission branching ratio (Ajello et al., 2010), and renormalization after Lyman Alpha measurements (Liu et al., 1998). We note that the scaled Ajello and Shemansky (1985) cross section agrees with the values recently reported by Ajello et al. (2020) within their estimated 35% uncertainty. While O I 135.6 nm (e + O) generally dominates the 135.6 nm bandpass, the (3,0) band of LBH does contribute to the total emission observed by GOLD. AURIC model calculations indicate that the (3,0) band can contribute nearly 50% of the integrated 135.6 nm intensity at low $\Sigma O/N_2$ and SZA. At larger SZA and $\Sigma O/N_2$ values the LBH contribution to the total 135.6 nm intensity is $\sim$10%. The lookup tables include the (3,0) contribution and so are consistent with observations.

As noted earlier, it is important to take into account instrument effects in order to create accurate lookup tables. The AURIC model is used to generate volume emission rates for atomic and LBH emissions. Franck-Condon and Hönl-London factors are used to produce a ro-vibrational line list (Budzien et al., 1994) that is scaled by the AURIC LBH volume emission rate. Finally, atomic emissions are added to this line list. The line list is passed through a software instrument model when constructing the lookup table. The instrument model converts input model spectra in physical units (Rayleighs

per Angstrom) to detector counts, then applies the appropriate line spread function and binning before converting back to physical units to simulate Level 1C spectra. In order to ensure consistency between the lookup table and observations, model 135.6 nm and LBH intensities in the lookup table are calculated from synthetic spectra using the same code that is used by the GOLD science data processing pipeline to calculate 135.6 nm and LBH intensities from observed Level 1C spectra.

The left hand panel of Figure 2 provides a graphical representation of the ON2 lookup table. Shown are curves of $\Sigma O/N_2$ as a function of 135.6/LBH intensity ratio for a range of solar zenith angles. Conceptually, given an observed intensity ratio it is possible to draw a line up from the abscissa until it intersects the curve corresponding to the solar zenith angle of the observation. The ordinate of this intersection is then $\Sigma O/N_2$ value for the observation. In practice the algorithm is vectorized and uses two dimensional interpolations on the intensity ratio and solar zenith angle grids to arrive at an $\Sigma O/N_2$ value.

3.2.1 Sources of Uncertainty

As noted above, a potential source of error in derived $\Sigma O/N_2$ is relative errors in cross sections. Cross section errors are assume to be ∼30%. A series of AURIC forward model runs was done in order to estimate the potential magnitude of the bias in $\Sigma O/N_2$ due to errors in cross sections. The cross sections for e+N_2 producing N2 LBH and e+ O producing O I 135.6 were independently scaled up and down by 30% (note that the O I 135.6 nm intensity changes even for the unscaled e + O cases because of the LBH band within the O I 135.6 nm bandpass). In the extreme cases the resulting $\Sigma O/N_2$ was 48% smaller than the unscaled $\Sigma O/N_2$ for LBH scaled up and 1356 scaled down, while at the other extreme $\Sigma O/N_2$ was 72% larger than the unscaled $\Sigma O/N_2$ for LBH scaled down and 1356 scaled up. Possible bias is ∼10% when both cross sections are scaled in the same direction. Additional bias could results from errors in the shape of the cross sections.

Nadir viewing geometry is assumed for the lookup tables with the assumption of constant SZA along the line-of-sight, which is valid for SZAs less than $\sim 80°$. For a fixed SZA the intensity ratio is constant to within a few percent for emission angles within 40° of nadir, where the emission angle is the angle between the vector normal to the refer-

ence ellipsoid of the observation point and the vector to GOLD. At an emission angle of 60°, the maximum error is $\sim 10\%$ relative to nadir viewing for large values of $\Sigma O/N_2$. Errors in 135.6 nm/LBH map to similar but smaller errors in $\Sigma O/N_2$. Typical values for random, systematic, and model uncertainties for GOLD $\Sigma O/N_2$ are discussed in Section 3.3.

3.2.2 Interpretation of $\Sigma O/N_2$

Since the introduction of the $\Sigma O/N_2$ concept in Strickland et al. (1995) there has been confusion as to what can be inferred about the atmosphere from this quantity (see, e.g., Zhang and Paxton (2011), Strickland et al. (2012), and Zhang and Paxton (2012), as well as a thorough discussion of on the meaning of $\Sigma O/N_2$ in Meier (2021)). One misconception originates from attaching undue importance to the N_2 reference depth, N_2^{ref}. There is no 'correct' value for the N_2 column density reference depth. The value should (1) be large enough to encompass most of the LBH emission and (2) minimize the uncertainty in $\Sigma O/N_2$ as a function of 135.6 nm/LBH. The latter condition can be restated as follows: the optimal reference depth should maximize the uniqueness of the 1-to-1 mapping between the 135.6 nm/LBH intensity ratio and $\Sigma O/N_2$. While Strickland et al. (1995) settled on a value of 10^{17} cm^{-2} for N_2^{ref}, the main effect of selecting a different reference column density is to change the estimated uncertainty when deriving $\Sigma O/N_2$ from observed intensity ratios (provided that condition (1) is satisfied). While the absolute value of the derived column density ratio will also change when using a different reference depth, this has little impact on previous results. $\Sigma O/N_2$ is always defined with respect to a certain reference depth. Strictly speaking, the reference depth should always be specified when presenting $\Sigma O/N_2$ values, either symbolically (e.g. $\Sigma O/N_2^{ref=10^{17}}$), or in text, as is customarily done. Therefore the fact that one derived $\Sigma O/N_2$ differs from another due to different values of N_2^{ref} is not significant. $\Sigma O/N_2$ is a measure of relative changes in the atmosphere and is most useful when comparing $\Sigma O/N_2$ values using the same N_2 reference depth. Note that a given N_2 reference column density is equivalent to a particular pressure level, so it may be conceptually more intuitive for some to think in terms of pressure levels. An N_2 reference column density of 10^{17} cm^{-2} is equivalent to $\sim$4 nanobar.

Another common conceptual error is attempting to infer composition information at a *particular altitude* from $\Sigma O/N_2$. Figure 3 displays composition parameters derived

from a range of NRLMSISE-00 model atmospheres (Picone et al., 2002). 1,814,400 model atmospheres were generated spanning the phase space of inputs:

1. Day of year: every 15 days
2. Time of day: every hour
3. Latitude: every 30 degrees
4. Longitude: every 30 degrees
5. Solar activity: low, medium, and high solar activity
6. Geomagnetic activity: 10 Ap values from 0 to 80

The top panel shows the value of Z_{ref}, the altitude where the N_2 column density reaches 10^{17} cm^{-2}. The middle and bottom panels show the atomic oxygen and molecular nitrogen number densities (cm^{-3}) at Z_{ref} (in black) and 150 km (in red). For a given $\Sigma O/N_2$ there is a range of possible values for Z_{ref} and volume number densities of O and N_2. For example, for $\Sigma O/N_2$ of 1.0, Z_{ref} has a 30 km range, while the densities of O and N_2 can vary by up to a factor of $\sim$3 for a given $\Sigma O/N_2$. While the model atmospheres may be scaled to ensure the model intensity ratio matches the observed one, narrowing the range of Z_{ref} and volume number densities of O and N_2, the point remains that $\Sigma O/N_2$ derived from remotely sensed UV dayglow can not be used to extract precise information about the atmosphere beyond the relative ratio of column O to column N_2. Furthermore, as demonstrated by Strickland et al. (1995), this relationship is not model dependent. The invocation of a particular model atmosphere to infer additional information about the state of the observed atmosphere moves the problem beyond the domain of purely remote sensing data analysis.

3.3 GOLD Level 2 ON2 Data Product

GOLD Level 2 ON2 files are NetCDF format files each containing data from one day. $\Sigma O/N_2$ and associated data (e.g. SZA, emission angle, etc.) are contained in three-dimensional arrays (# longitudes $\times$ # latitudes $\times$ # of DAY scans). The longitude and latitude grids are constant for all scans and are contained in two separate two-dimensional arrays. Level 1 processing takes into account small variations in pointing when binning all DAY observations onto a fixed grid. The Level 1C spatial grid is defined as a constant 0.2° grid with respect to satellite look angles, which yields a non-uniform grid when projected to longitude-latitude coordinates. The spatial resolution of L1C is 125 $\times$ 125

326 km^2 at nadir. Before ingestion by the ON2 algorithm, L1C data is spatially binned 2 ×
327 2 (i.e. 4 L1C spatial pixels) to create an L2 spatial pixel with a 250 × 250 km^2 spatial
328 resolution at nadir. This binning ensures better signal to noise and provides ON2 data
329 on the same grid as GOLD Level 2 TDISK data. The number of DAY scans can vary
330 somewhat from day to day and is used as NetCDF's unlimited dimension (allowing for
331 concatenation of files by various NetCDF utilities).

332 Uncertainty values are reported for the input intensities and derived $\Sigma O/N_2$ and
333 are separated into random, systematic, and model uncertainties (the latter uncertainty
334 does not apply to the input radiances). These uncertainties begin with values contained
335 in Level 1C files and are calculated using a rigorous propagation of errors (Evans et al.,
336 1995). Typical random uncertainties are $\sim 5\%$. Uncertainties at this level are small enough
337 to allow short and long term variability to be observed (discussed in Section 1). System-
338 atic uncertainties are based on the systematic uncertainties reported in the Level 1C files
339 and represent a $\sim$5% bias. The model uncertainty is an estimate of the potential bias
340 in derived ON2 due to uncertainties in the relevant cross sections. Values for this quan-
341 tity are in the 30% to 40% range.

342 LBH measurements by previous missions have typically included as much of the
343 LBH band system in the measured bandpass as practical in order to maximize total sig-
344 nal. In addition most instruments before GOLD did not have the wavelength resolution
345 necessary to effectively isolate particular bands. The relative intensity of LBH bands long-
346 ward of $\sim$150 nm decreases enough that including them in the total LBH bandpass in-
347 creases the total signal but does not significantly improve the signal to noise ratio (SNR).
348 In other words, including this part of the spectrum adds nearly as much noise as it does
349 signal to the measured LBH. Therefore an LBH bandpass of 140.5 nm – 148.0 nm was
350 selected for GOLD to maximize SNR. The bright (2,0) band at 138.4 nm is not included
351 in the LBH bandpass at this time due to concerns about sensitivity decreases from in-
352 strument degradation at 138.4 nm in addition to those at 135.6 nm (see Section 3.4).

353 Level 2 files contain arrays that specify the bandpasses used for calculating the 135.6
354 nm and LBH broadband intensities. These Boolean mask arrays are reported on an over-
355 sampled wavelength grid (0.01 nm compared with the native Level 1C wavelength grid
356 of 0.04 nm) to allow straightforward calculation and comparison of 135.6 nm and LBH
357 broadband intensities from any non-GOLD data set.

Data quality indicator (DQI) arrays are used to note potential problems with derived $\Sigma O/N_2$ data in the Level 2 files. The DQI arrays contain a value for each spatial pixel, with a value of zero for no known problems. Values greater than zero indicate that one or more data quality flags have been set for that pixel. The reported DQI values are a bitwise combination of individual flags so that a single number can be used to specify which of many possible flags are set. For example, a DQI value of 131 indicates that bits 1, 2, and 8 are set (i.e. they are equal to 1 since 131 = `10000011`). Given the bitwise combination of DQI values, it is possible that the addition of new flags or refinements to the algorithms used to set each flag may change DQI values between versions. The end user is advised to refer to the documentation and release notes (available at https://gold.cs.ucf.edu/) accompanying each version for the appropriate list of DQI values.

Figure 4 presents a sample of Level 2 ON2 data. Shown in the left and middle panel are $\Sigma O/N_2$ values from 13 and 14 May 2019 (day of year 133 and 134). Both images combine the north and south hemisphere scans performed at 10:40 and 10:52 UT. The average value is used for pixels in the region where the scans overlap near the equator. Emission angle from a given pixel to the spacecraft is essentially constant for all scans (0° at the subspacecraft point and $\sim 90°$ at the limb). The effects of a geomagnetic storm can be seen in the DOY 134 image. The storm began about 03:00 UT on DOY 134 and reached a Kp of 7 during the 06:00-08:00 UT time period. The resulting depletion of $\Sigma O/N_2$ at higher latitudes and enhanced $\Sigma O/N_2$ at lower latitudes was first seen by Drob et al. (1999) and Strickland et al. (1999), and has been observed with GOLD data (Cai et al., 2020). The right hand panel shows the percent change in $\Sigma O/N_2$ from pre-storm to storm. A sequence of images showing the temporal evolution of $\Sigma O/N_2$ over the course of 3 days encompassing the storm is available as Supporting Information for this paper.

Derived $\Sigma O/N_2$ from high latitudes near the auroral region must be treated with care. Energetic particle precipitation produces 135.6 nm and LBH emission (e.g., Strickland et al., 1983, 1993) from a source that is not included in the lookup table, which assumes dayglow from excitation by photoelectron impact only. Similarly, O^+ radiative recombination (RR) within the equatorial ionization anomalies (EIA) produces 135.6 nm emission that can result in an erroneously large $\Sigma O/N_2$. This ionospheric contribution to measured 135.6 can be incorrectly attributed to variability in the neutral atmosphere (Kil et al., 2013). During periods of low solar and geomagnetic activity (such as the first few years of the GOLD mission) the RR source is a minor contribution to the measured

135.6 nm signal, typically on the order of 10 Rayleighs, or a $\sim 1-2$ % for a wide range of solar zenith and emission angles. The fraction of O I 135.6 nm emission from RR maps to a similar error in $\Sigma O/N_2$ and so a few percent error can be attributed to RR for most conditions observed by GOLD to date. It is important to emphasize that these are only average values for the low geomagnetic activity conditions prevailing during the GOLD mission to date and the RR source will become a more significant fraction of the measured 135.6 nm as geomagnetic activity increases during Solar Cycle 25, with a potential contribution of a few hundred Rayleighs, resulting in a $10-20$ % or potentially larger error in $\Sigma O/N_2$ (Lee et al., 2013). Further details on estimates of the RR source contribution are provided in the Supporting Information accompanying this paper. Level 2 ON2 files currently available (version 3 as of this writing) do not set DQI flags for possible contamination due to auroral or RR sources.

3.4 Data Quality Issues

The lookup tables are constructed with the assumption that instrument artifacts are removed from Level 1C data (only random noise is expected to be present). Any artifacts not correctly accounted for in Level 1C data can impact the accuracy of derived $\Sigma O/N_2$ values. Users of GOLD ON2 data should be aware of several instrument artifacts that may be present to avoid misinterpreting them as real geophysical variations.

The first artifact is background due to radiation. In geostationary orbit, GOLD is exposed to a radiation environment that is highly variable on both short and long term time scales. Energetic particle flux can vary by over two orders of magnitude. These energetic particles produce gamma rays when they are stopped in the detector (i.e. bremsstrahlung). At the lower end of the range of particle fluxes, the background is essentially negligible while at the high end the background can account for $\sim$30% of the broadband LBH intensity, if uncorrected.

The second artifact is detector sensitivity changes ('gain sag'), especially problematic with the bright 135.6 nm emission. This degradation is accounted for in GOLD Level 1 processing through a flat fielding procedure. However, the degradation eventually becomes large enough that the flat field correction would be inadequate. This effect is known to occur with MCP detectors thus GOLD was designed with a grating yaw mechanism (GYM) that allows the spectral image on the detector to be shifted. The GYM is moved

so that the 135.6 nm line falls on a different part of the detector. As of this writing five GYM shifts have been implemented for GOLD Channel A, from which all ON2 and QEUV data are derived. ON2 data near these GYM shifts should be treated with caution as there may be systematic shifts in the magnitude of ON2 the order of ∼15% between the time periods (days to weeks) just before and after a shift. Users should refer to Release Notes on the SDC page (https://gold.cs.ucf.edu/) for a more detailed discussion and most up to date information.

Another important issue to be aware of when interpreting data is variation in sensitivity along the slit. The flatfield correction attempts to take into account variations in both the spectral and spatial (along slit) dimensions. Variation in along-slit sensitivity creates a bias in the North-South direction. A maximum bias of ∼10% is seen when comparing pixels near the equator from sequential North/South hemisphere scans because these pixels are sampled by opposite ends of the slit.

Incomplete background removal can lead to an overestimation of measured intensities, while inadequate flat fielding may produce either an under or overestimation of 135.6 nm intensity. Thus it is important to be cognizant of these artifacts when spatial and temporal variations in data products are being studied. Users of the data are strongly encouraged to contact the authors or PI in order to be fully aware of possible impacts of instrument artifacts to their science.

4 Q_{EUV}

4.1 Algorithm

Q_{EUV} derived from FUV airglow data is defined to be the solar energy flux between 1 and 45 nm that is incident on the upper atmosphere. This cutoff is selected since solar photons longward of 45 nm do not contribute significantly to FUV dayglow via photoelectron production (Strickland et al., 1995). Lookup tables similar to those described in Section 3.2 are constructed for Q_{EUV}. The main difference is that inputs for the algorithm in this case are $\Sigma O/N_2$ and an absolute intensity (the intensity ratio 135.6 nm/LBH could be used in place of $\Sigma O/N_2$). While either the 135.6 nm or LBH intensity could be used when constructing the table, the 135.6 nm intensity is used for its simple bandpass and higher signal to noise. Given $\Sigma O/N_2$, an absolute intensity, and the SZA of the

observation point, the curves in the right panel of Figure 2 can be used to derive Q_{EUV}. The expression in terms of 135.6 nm is

$$Q_{\mathrm{EUV}} = \frac{I_{obs}^{135.6} \cdot \cos\theta}{I_{table}^{135.6}} Q_{\mathrm{EUV}}^{ref} \tag{3}$$

where the numerator contains the observed 135.6 nm intensity, θ is the emission angle of the observed location, and the denominator is the 135.6 nm intensity interpolated from the lookup table for the observed $\Sigma O/N_2$ and associated SZA. The Q_{EUV}^{ref} of the solar spectrum used to generate the lookup table (1.59 erg $cm^{-2}s^{-1}$) is then scaled by the ratio of the observed to lookup table intensities to arrive at the observed Q_{EUV}.

AURIC column emission rates are calculated for nadir viewing gemoetry when constructing lookup tables. As previously noted, this does not present a problem for the $\Sigma O/N_2$ algorithm because increases in brightness due to increased path length are present in both the numerator and the denominator of the intensity ratio and effectively cancel out. On the other hand, Q_{EUV} in Equation 3 is directly proportional to the absolute intensity and is therefore sensitive to the emission angle. The current algorithm corrects for this increase in brightness due to greater path length by scaling the absolute intensity by the cosine of the emission angle. This approximation breaks down for large emission angles, so Q_{EUV} is not calculated for disk pixels with an emission angle greater than 75°.

4.2 GOLD Level 2 QEUV Data Product

The QEUV Level 2 data product is derived from Level 1C DAY data. Q_{EUV} is a measure of solar energy input and therefore has no geospatial component, so calculating Q_{EUV} for simultaneously observed but widely separated locations should return essentially the same Q_{EUV} value (within the limits allowed by the noise of the input data). Therefore, the QEUV data product is a time series of Q_{EUV} values. For each DAY scan a single row of Level 1C pixels is used to derive Q_{EUV}. A row of L1C data runs in the East-West direction at a more or less constant latitude. Each row corresponds to a fixed location along the slit as it is moved across the disk in time. Within a scan the time resolution is ∼8 seconds with a 2 – 5 minute gap between scans. For scans of the northern hemisphere the row closest to 30°N is used, while for the southern hemisphere the row closest to 37.5°S is selected. The latitudes selected for calculating Q_{EUV} are balanced between the desire to maximize temporal coverage available from pixels near the equa-

tor while also being far enough away from the equatorial ionization anomaly to minimize contamination of 135.6 nm by radiative recombination. The asymmetry between the two hemispheres is due to the location of the magnetic equator within GOLD's field of view. The magnetic equator crosses the geographic equator close to GOLD's subsatellite point. To the west of the subsatellite point the magnetic equator is south of the geographic equator, while to the east of the subsatellite point the magnetic equator is north of the geographic equator. The magnetic equator is farther to the south on the western side than it is to the north on the eastern side within GOLD's field of view.

As with the ON2 data product, random, systematic, and model uncertainty values are reported for the input intensities and derived QEUV (the model uncertainty does not apply to the input radiances). For QEUV, typical random uncertainties are between 5% to 15%. Systematic uncertainties are based on the systematic uncertainties reported in the Level 1C files and are ∼6%. Model uncertainties are in the 25% to 30% range and are driven by uncertainties in the relevant cross sections. Any data quality issues that affect ON2 will also affect QEUV since ON2 is an input for deriving QEUV. As with ON2, there is ∼10% bias between QEUV derived from North and South hemisphere scans due to variations in along slit sensitivity.

Figure 5 presents a sample of GOLD QEUV data. The upper panel shows Q_{EUV} from the spacecraft local noon DAY disk scan on 8 November 2018. The middle panel shows all Q_{EUV} values from that day. The increased spread in values at early and late times is due to a combination of larger solar zenith and emission angles. The lower panel shows the daily averaged Q_{EUV} and F10.7 since the start of GOLD's science mission. Despite the low solar activity, the mean Q_{EUV} values are well correlated with F10.7.

5 Summary

In this report we have presented an overview of GOLD ON2 and QEUV data products. Though the basic algorithms involved have been previously well validated, they require adjustments for application to the GOLD data set. GOLD's vantage point from geostationary orbit also provides a large scale, high cadence, synoptic view for most of each day. Such observations were unavailable to earlier missions. Users of GOLD data are reminded to carefully read documentation and release notes for detailed information

regarding DQI flag values, limitations of the data, etc. Representative Level 1C and 2 data demonstrate the potential for new science, enabled by GOLD.

Acronyms

AURIC Atmospheric Ultraviolet Radiance Integrated Code

GOLD Global-scale Observations of Limb and Disk

GYM grating yaw mechanism

LBH Lyman-Birge-Hopfield

MCP micro channel plate

RR radiative recombination

SZA solar zenith angle

Notation

$\Sigma O/N_2$ The ratio of the vertical column density of atomic oxygen above the altitude where the column density of molecular nitrogen is equal to the reference depth. A more accurate expression would be of the general form $\Sigma O/\Sigma N_2$. Clearly this would be cumbersome to use repeatedly, therefore we adopt the notation $\Sigma O/N_2$. This notation is preferred to simply O/N_2, which is ambiguous and may be confused with the volume density ratio at a specific altitude (which should be written as $[O]/[N_2]$).

ON2 GOLD Level 2 data product containing $\Sigma O/N_2$ derived from dayglow measurements.

Q_{EUV} Integrated solar flux between 1 and 45 nm.

QEUV GOLD Level 2 data product containing Q_{EUV} values derived from dayglow measurements.

Acknowledgments

We thank Doug Strickland and Bob Meier for many years of interesting discussions about $\Sigma O/N_2$. Thanks to Doug Strickland as well for reading and suggesting improvements to the manuscript. We are indebted to the Science Data Center teams at LASP and the University of Central Florida, particularly Connie Harper. We thank Mihail Codrescu

and Mariangel Fedrizzi for providing CTIPe model output used during development and testing of the algorithms, as well as Stan Solomon for assistance navigating the publication process. GNU Parallel (Tange, 2018) was used to drastically reduce computational time necessary to construct look up tables. GOLD Level 1C and 2 data used in this paper can be found at the GOLD website, https://gold.cs.ucf.edu/ and NASA's Space Physics Data Facility, https://spdf.gsfc.nasa.gov. This work was supported by NASA contract 80GSFC18C0061.

References

Ajello, J., Mangina, R., & Meier, R. (2010). UV molecular spectroscopy from electron impact for applications to planetary atmospheres and astrophysics. *IN HATANO, Y., KATSUMURA, Y. & MOZUMDER, A.(Eds.) Charged Particle and Photon Interactions with Matter: Recent Advances, Applications, and Interfaces*.

Ajello, J. M., Evans, J. S., Veibell, V., Malone, C. P., Holsclaw, G. M., Hoskins, A. C., ... others (2020). The uv spectrum of the lyman-birge-hopfield band system of n2 induced by cascading from electron impact. *Journal of Geophysical Research: Space Physics*, *125*(3), e2019JA027546.

Ajello, J. M., & Shemansky, D. E. (1985, October). A reexamination of important N_2 cross sections by electron impact with application to the dayglow - The Lyman-Birge-Hopfield band system and N I (1199.99 nm). *J. Geophys. Res.*, *90*, 9845–9861. doi: 10.1029/JA090iA10p09845

Aryal, S., Evans, J. S., Correira, J., Burns, A. G., Wang, W., Solomon, S. C., ... Jee, G. (2020, September). First Global-Scale Synoptic Imaging of Solar Eclipse Effects in the Thermosphere. *Journal of Geophysical Research (Space Physics)*, *125*(9), e27789. doi: 10.1029/2020JA027789

Bishop, J., & Feldman, P. D. (2003, June). Analysis of the Astro-1/Hopkins Ultraviolet Telescope EUV-FUV dayside nadir spectral radiance measurements. *Journal of Geophysical Research (Space Physics)*, *108*, 1243. doi: 10.1029/2001JA000330

Budzien, S., Feldman, P., & Conway, R. (1994). Observations of the far ultraviolet airglow by the ultraviolet limb imaging experiment on sts-39. *Journal of Geophysical Research: Space Physics*, *99*(A12), 23275–23287.

Cai, X., Burns, A. G., Wang, W., Qian, L., Solomon, S. C., Eastes, R. W., ... McClintock, W. E. (2020, September). The Two-Dimensional Evolution of Thermospheric $\sum O/N_2$ Response to Weak Geomagnetic Activity During Solar-Minimum Observed by GOLD. *Geophysical Research Letters*, *47*(18), e88838. doi: 10.1029/2020GL088838

Conway, R. R. (1982, Feb). Self-absorption of the N_2 Lyman-Birge-Hopfield bands in the far ultraviolet dayglow. *J. Geophys. Res.*, *87*(A2), 859-866. doi: 10.1029/JA087iA02p00859

Craven, J. D., Nicholas, A. C., Frank, L. A., Strickland , D. J., & Immel, T. J. (1994, Dec). Variations in the FUV dayglow after intense auroral activity. *Geophys. Res. Lett.*, *21*(25), 2793-2796. doi: 10.1029/94GL02458

Crowley, G., Hackert, C. L., Meier, R. R., Strickland, D. J., Paxton, L. J., Pi, X., ... Wene, G. (2006, October). Global thermosphere-ionosphere response to onset of 20 November 2003 magnetic storm. *Journal of Geophysical Research (Space Physics)*, *111*(A10), 10. doi: 10.1029/2005JA011518

Crowley, G., Reynolds, A., Thayer, J., Lei, J., Paxton, L., Christensen, A., ... Strickland, D. (2008). Periodic modulations in thermospheric composition by solar wind high speed streams. *Geophysical Research Letters*, *35*(21).

Drob, D., Meier, R., Picone, J., Strickland, D., Cox, R., & Nicholas, A. (1999). Atomic oxygen in the thermosphere during the july 13, 1982, solar proton event deduced from far ultraviolet images. *Journal of Geophysical Research: Space Physics*, *104*(A3), 4267–4278.

Eastes, R. W. (2000, August). Modeling the N_2 Lyman-Birge-Hopfield bands in the dayglow: Including radiative and collisional cascading between the singlet states. *J. Geophys. Res.*, *105*, 18557–18574. doi: 10.1029/1999JA000378

Eastes, R. W., McClintock, W. E., Burns, A. G., Anderson, D. N., Andersson, L., Aryal, S., ... Woods, T. N. (2020, July). Initial Observations by the GOLD Mission. *Journal of Geophysical Research (Space Physics)*, *125*(7), e27823. doi: 10.1029/2020JA027823

Eastes, R. W., McClintock, W. E., Burns, A. G., Anderson, D. N., Andersson, L., Codrescu, M., ... Oberheide, J. (2017, August). The global-scale observations of the limb and disk (GOLD) mission. *Space Science Reviews*, *212*(1-2), 383–408. doi: 10.1007/s11214-017-0392-2

Eastes, R. W., Solomon, S. C., Daniell, R. E., Anderson, D. N., Burns, A. G., England, S. L., ... McClintock, W. E. (2019). Global-scale observations of the equatorial ionization anomaly. *Geophysical Research Letters*, *46*(16), 9318-9326. doi: 10.1029/2019GL084199

Evans, J. S., Strickland, D. J., & Huffman, R. E. (1995, July). Satellite remote sensing of thermospheric O/N_2 and solar EUV. 2: Data analysis. *J. Geophys. Res.*, *100*, 12227. doi: 10.1029/95JA00573

Gladstone, G. R. (1982, May). Radiative transfer with partial frequency re-

distribution in inhomogeneous atmospheres - application to the jovian aurora. *J. Quant. Spectrosc. Radiat. Transfer*, *27*, 545-556. doi: 10.1016/0022-4073(82)90107-8

Gladstone, G. R. (1988, December). Uv resonance line dayglow emissions on earth and jupiter. *J. Geophys. Res.*, *93*, 14623-14630. doi: 10.1029/JA093iA12p14623

Hanson, W. B. (1969, July). Radiative recombination of atomic oxygen ions in the nighttime F region. *Journal of Geophysical Research*, *74*(14), 3720-3722. doi: 10.1029/JA074i014p03720

Hinteregger, H. E., Fukui, K., & Gilson, B. R. (1981, Nov). Observational, reference and model data on solar EUV, from measurements on AE-E. *Geophys. Res. Lett.*, *8*(11), 1147-1150. doi: 10.1029/GL008i011p01147

Immel, T. J., Craven, J. D., & Frank, L. A. (1997, Apr). Influence of IMF B_y on large-scale decreases of O column density at middle latitudes. *Journal of Atmospheric and Solar-Terrestrial Physics*, *59*, 725-737. doi: 10.1016/S1364-6826(96)00099-5

Immel, T. J., Crowley, G., Craven, J. D., & Roble, R. G. (2001, Aug). Dayside enhancements of thermospheric O/N_2 following magnetic storm onset. *J. Geophys. Res.*, *106*(A8), 15471-15488. doi: 10.1029/2000JA000096

Kanik, I., Noren, C., Makarov, O. P., Vattipalle, P., Ajello, J. M., & Shemansky, D. E. (2003, November). Electron impact dissociative excitation of o_2: 2. absolute emission cross sections of the oi(130.4 nm) and oi(135.6 nm) lines. *Journal of Geophysical Research (Planets)*, *108*, 5126. doi: 10.1029/2000JE001423

Kil, H., Lee, W. K., Shim, J., Paxton, L. J., & Zhang, Y. (2013, February). The effect of the 135.6 nm emission originated from the ionosphere on the TIMED/GUVI O/N_2 ratio. *Journal of Geophysical Research (Space Physics)*, *118*, 859–865. doi: 10.1029/2012JA018112

Lee, W. K., Kil, H., Paxton, L. J., Zhang, Y., & Shim, J. S. (2013). The effect of geomagnetic-storm-induced enhancements to ionospheric emissions on the interpretation of the timed/guvi o/n2 ratio. *Journal of Geophysical Research: Space Physics*, *118*(12), 7834–7840.

Liu, X., Shemansky, D. E., Ahmed, S. M., James, G. K., & Ajello, J. M. (1998, November). Electron-impact excitation and emission cross sections of the

h_2 lyman and werner systems. *J. Geophys. Res.*, *103*, 26739-26758. doi: 10.1029/98JA02721

Lumpe, J. D., McClintock, W. E., Evans, J. S., Correira, J., Veibell, V., Beland, S., & Eastes, R. (2020, April). A New Data Set of Thermospheric Molecular Oxygen From the Global-scale Observations of the Limb and Disk (GOLD) Mission. *Journal of Geophysical Research (Space Physics)*, *125*(4), e27812. doi: 10.1029/2020JA027812

McClintock, W. E., Eastes, R. W., Beland , S., Bryant, K. B., Burns, A. G., Correira, J., ... Veibel, V. (2020, May). Global-Scale Observations of the Limb and Disk Mission Implementation: 2. Observations, Data Pipeline, and Level 1 Data Products. *Journal of Geophysical Research (Space Physics)*, *125*(5), e27809. doi: 10.1029/2020JA027809

Meier, R. R. (1991). Ultraviolet spectroscopy and remote sensing of the upper atmosphere. *Space Sci. Rev.*, *58*, 1–185. doi: 10.1007/BF01206000

Meier, R. R. (2021, March). The Thermospheric Column O/N_2 Ratio. *Journal of Geophysical Research (Space Physics)*, *126*(3), e29059. doi: 10.1029/2020JA029059

Meier, R. R., Crowley, G., Strickland, D. J., Christensen, A. B., Paxton, L. J., Morrison, D., & Hackert, C. L. (2005, August). First look at the 20 November 2003 superstorm with TIMED/GUVI: Comparisons with a thermospheric global circulation model. *Journal of Geophysical Research (Space Physics)*, *110*(A9), 9. doi: 10.1029/2004JA010990

Meier, R. R., Samson, J. A. R., Chung, Y., Lee, E.-M., & He, Z.-X. (1991, August). Production of N^{+*} from $N_2 + h\nu$ - Effective EUV emission yields from laboratory and dayglow data. *Planet. Space Sci.*, *39*, 1197–1207. doi: 10.1016/0032-0633(91)90171-6

Meléndez-Alvira, D. J., Meier, R. R., Picone, J. M., Feldman, P. D., & McLaughlin, B. M. (1999, July). Analysis of the oxygen nightglow measured by the Hopkins Ultraviolet Telescope: Implications for ionospheric partial radiative recombination rate coefficients. *Journal of Geophysical Research*, *104*(A7), 14901-14914. doi: 10.1029/1999JA900136

Nicholas, A. C., Craven, J. D., & Frank, L. A. (1997, Mar). A survey of large-scale variations in thermospheric oxygen column density with magnetic activity as

inferred from observations of the FUV dayglow. *J. Geophys. Res.*, *102*(A3), 4493-4510. doi: 10.1029/96JA03464

Oberheide, J., Pedatella, N. M., Gan, Q., Kumari, K., Burns, A. G., & Eastes, R. W. (2020, January). Thermospheric Composition O/N_2 Response to an Altered Meridional Mean Circulation During Sudden Stratospheric Warmings Observed by GOLD. *Geophysical Research Letters*, *47*(1), e86313. doi: 10.1029/2019GL086313

Picone, J. M., Hedin, A. E., Drob, D. P., & Aikin, A. C. (2002, December). NRLMSISE-00 empirical model of the atmosphere: Statistical comparisons and scientific issues. *Journal of Geophysical Research (Space Physics)*, *107*, 1468. doi: 10.1029/2002JA009430

Romero-Hernandez, E., Denardini, C. M., Takahashi, H., Gonzalez-Esparza, J. A., Nogueira, P. A. B., de Pádua, M. B., ... Aguilar-Rodriguez, E. (2018, December). Daytime Ionospheric TEC Weather Study Over Latin America. *Journal of Geophysical Research (Space Physics)*, *123*(12), 10,345-10,357. doi: 10.1029/2018JA025943

Schunk, R., & Nagy, A. (2009). *Ionospheres: physics, plasma physics, and chemistry.* Cambridge university press.

Strickland, D., Cox, R., Meier, R., & Drob, D. (1999). Global o/n2 derived from de 1 fuv dayglow data: Technique and examples from two storm periods. *Journal of Geophysical Research: Space Physics*, *104*(A3), 4251–4266.

Strickland, D. J. (2001, Dec). Six days of thermospheric-ionospheric weather over the Northern Hemisphere in late September 1981. *J. Geophys. Res.*, *106*(A12), 30291-30306. doi: 10.1029/2001JA001113

Strickland, D. J., Bishop, J., Evans, J. S., Majeed, T., Shen, P. M., Cox, R. J., ... Huffman, R. E. (1999, August). Atmospheric ultraviolet radiance integrated code (AURIC): theory, software architecture, inputs, and selected results. *Journal of Quantitative Spectroscopy and Radiative Transfer*, *62*(6), 689-742. doi: 10.1016/S0022-4073(98)00098-3

Strickland, D. J., Cox, R. J., Meier, R. R., & Drob, D. P. (1999, Mar). Global O/N_2 derived from DE 1 FUV dayglow data: Technique and examples from two storm periods. *J. Geophys. Res.*, *104*(A3), 4251-4266. doi: 10.1029/98JA02817

Strickland, D. J., Daniell, J., R. E., Jasperse, J. R., & Basu, B. (1993, Dec). Transport-theoretic model for the electron-proton-hydrogen atom aurora 2. Model results. *J. Geophys. Res.*, *98*(A12), 21533-21548. doi: 10.1029/93JA01645

Strickland, D. J., Daniell, R. E., & Craven, J. D. (2001, Oct). Negative ionospheric storm coincident with DE 1-observed thermospheric disturbance on October 14, 1981. *J. Geophys. Res.*, *106*(A10), 21049-21062. doi: 10.1029/2000JA000209

Strickland, D. J., Evans, J. S., & Correira, J. (2012, July). Comment on "Long-term variation in the thermosphere: TIMED/GUVI observations" by Y. Zhang and L. J. Paxton. *Journal of Geophysical Research (Space Physics)*, *117*, 7302. doi: 10.1029/2011JA017350

Strickland, D. J., Evans, J. S., & Paxton, L. J. (1995). Satellite remote sensing of thermospheric O/N_2 and solar EUV. 1: Theory. *J. Geophys. Res.*, *100*, 12217. doi: 10.1029/95JA00574

Strickland, D. J., Jasperse, J. R., & Whallen, J. A. (1983, Oct). Dependence of auroral FUV emissions on the incident electron spectrum and neutral atmosphere. *J. Geophys. Res.*, *88*(A10), 8051-8062. doi: 10.1029/JA088iA10p08051

Strickland, D. J., Lean, J. L., Daniell, R. E., Knight, H. K., Woo, W. K., Meier, R. R., ... Paxton, L. J. (2007, June). Constraining and validating the Oct/Nov 2003 X-class EUV flare enhancements with observations of FUV dayglow and E-region electron densities. *Journal of Geophysical Research (Space Physics)*, *112*(A11), 6313. doi: 10.1029/2006JA012074

Strickland, D. J., Lean, J. L., Meier, R. R., Christensen, A. B., Paxton, L. J., Morrison, D., ... McMullin, D. R. (2004, February). Solar EUV irradiance variability derived from terrestrial far ultraviolet dayglow observations. *Geophys. Res. Lett.*, *31*, 3801. doi: 10.1029/2003GL018415

Strickland, D. J., Link, R., & Paxton, L. J. (1993, January). FUV remote sensing of thermospheric composition and the solar euv flux. In R. E. Huffman (Ed.), *Ultraviolet technology iv* (Vol. 1764, p. 117-131). doi: 10.1117/12.140842

Strickland, D. J., Meier, R. R., Walterscheid, R. L., Craven, J. D., Christensen, A. B., Paxton, L. J., ... Crowley, G. (2004, January). Quiet-time sea-

sonal behavior of the thermosphere seen in the far ultraviolet dayglow. *Journal of Geophysical Research (Space Physics)*, *109*(A18), 1302. doi: 10.1029/2003JA010220

Tange, O. (2018). *Gnu parallel 2018*. Ole Tange. Retrieved from `https://doi.org/10.5281/zenodo.1146014` doi: 10.5281/zenodo.1146014

Tinsley, B. A., Christensen, A. B., Bittencourt, J., Gouveia, H., Angreji, P. D., & Takahashi, H. (1973, January). Excitation of oxygen permitted line emissions in the tropical nightglow. *Journal of Geophysical Research*, *78*(7), 1174. doi: 10.1029/JA078i007p01174

Warren, H. P. (2005, March). A Solar Minimum Irradiance Spectrum for Wavelengths below 1200 Å. *Ap. J. Supp. Ser.*, *157*, 147–173. doi: 10.1086/427171

Woods, T. N., Chamberlin, P. C., Peterson, W. K., Meier, R. R., Richards, P. G., Strickland, D. J., ... Tsurutani, B. T. (2008, August). XUV Photometer System (XPS): Improved Solar Irradiance Algorithm Using CHIANTI Spectral Models. *Solar Physics*, *250*, 235–267. doi: 10.1007/s11207-008-9196-6

Woods, T. N., Rottman, G. J., Bailey, S. M., Solomon, S. C., & Worden, J. R. (1998, Jan). Solar Extreme Ultraviolet Irradiance Measurements During Solar Cycle 22. *solphys*, *177*, 133-146. doi: 10.1023/A:1004912310883

Zhang, Y., & Paxton, L. J. (2011, April). Long-term variation in the thermosphere: TIMED/GUVI observations. *Journal of Geophysical Research (Space Physics)*, *116*(A15), 0. doi: 10.1029/2010JA016337

Zhang, Y., & Paxton, L. J. (2012, July). Reply to comment by d.j. strickland et al. on "long-term variation in the thermosphere: Timed/guvi observations". *Journal of Geophysical Research (Space Physics)*, *117*, A07304. doi: 10.1029/2012JA017594

Zhang, Y., Paxton, L. J., Morrison, D., & Schaefer, B. (2018, Apr). Storm-time variations of atomic nitrogen 149.3 nm emission. *Journal of Atmospheric and Solar-Terrestrial Physics*, *169*, 78-82. doi: 10.1016/j.jastp.2018.01.023

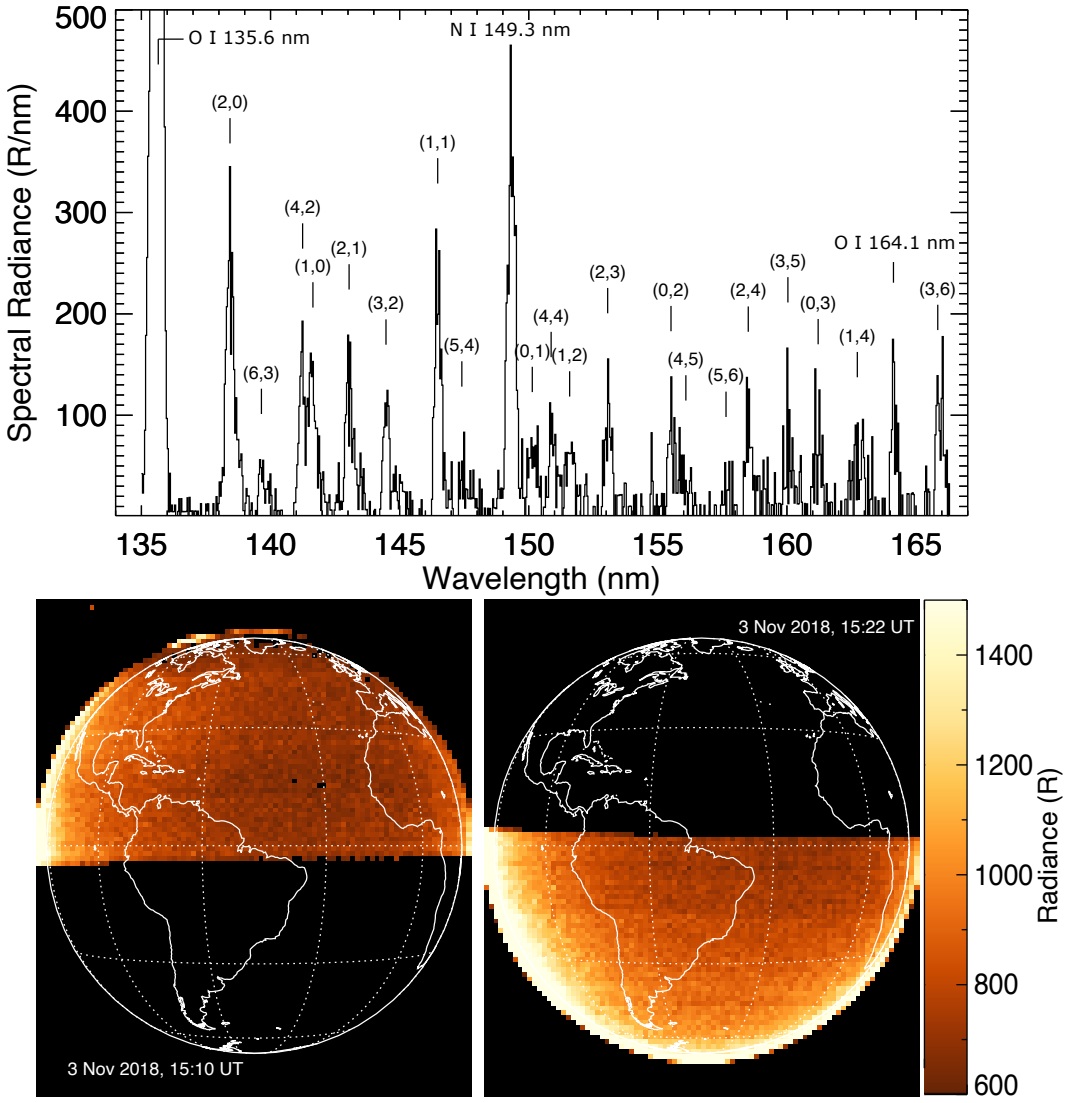

Figure 1. Upper panel: Typical binned spectrum used with ON2 algorithm. Identified are three atomic emission features as well as prominent N_2 Lyman-Birge-Hopfield bands. Lower panel: Sample of 135.6 nm intensity measured during typical DAY scan. Times shown indicate the start time of the observation, which begins on the east limb and scans to the west limb over the course of 12 minutes. Note that L1C DAY scans are binned 2x2 before being used by the ON2 algorithm.

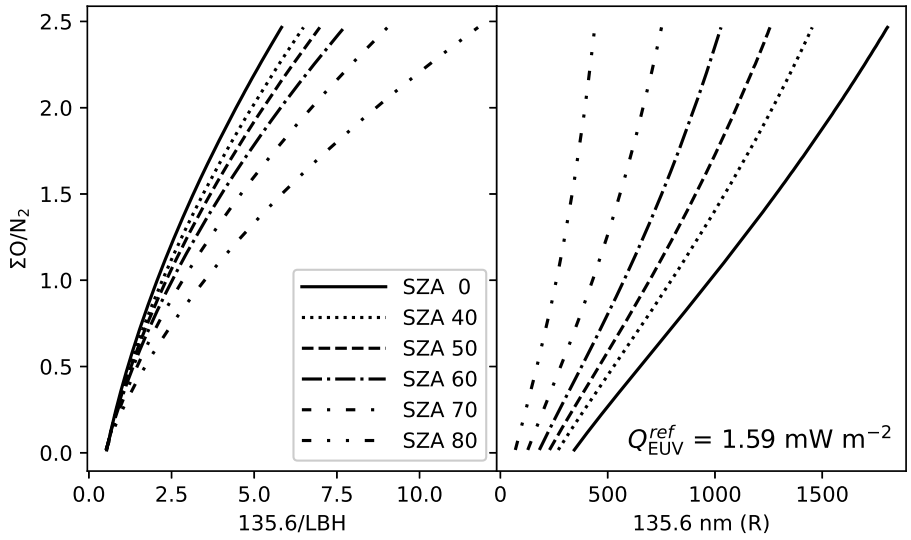

Figure 2. Left panel: Graphical representation of ON2 lookup table, showing $\Sigma O/N_2$ versus 135.6 nm/LBH and solar zenith angle. Right panel: Graphical representation of QEUV lookup table, showing $\Sigma O/N_2$ as a function of 135.6 nm intensity for a range of solar zenith angles.

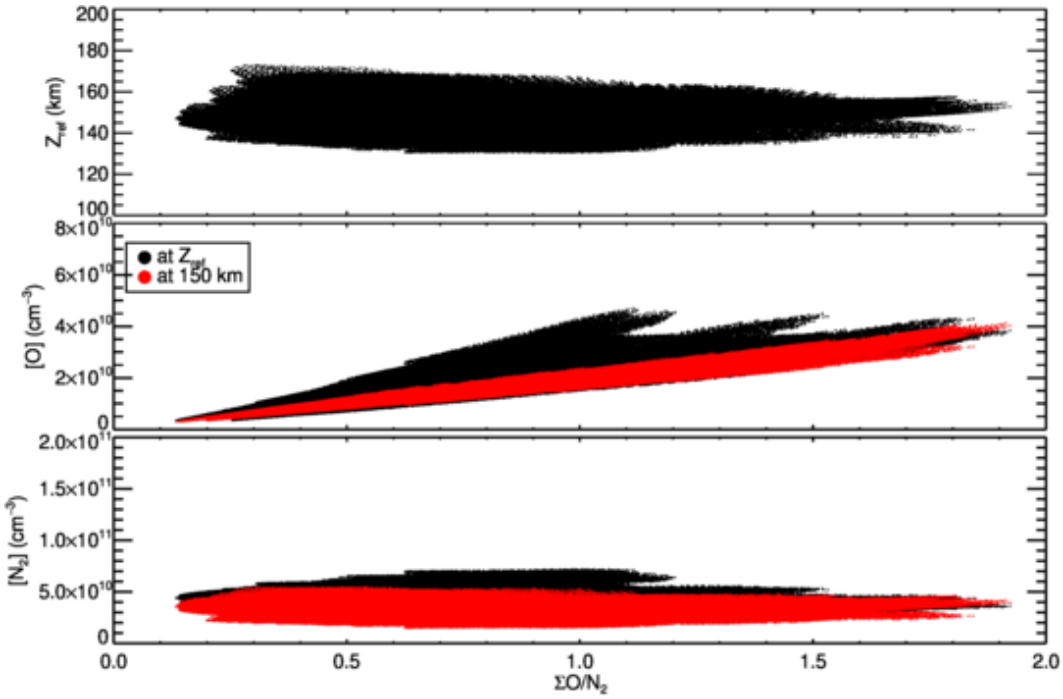

Figure 3. Model atmospheric composition parameters shown as a function of $\Sigma O/N_2$ for a wide range of NRLMSISE-00 model atmospheres. Upper panel shows Z_{ref}, while the middle and lower panels show atomic oxygen and molecular nitrogen number densities, respectively, at Z_{ref} (black) and 150 km (red). Dots indicate individual model atmospheres.

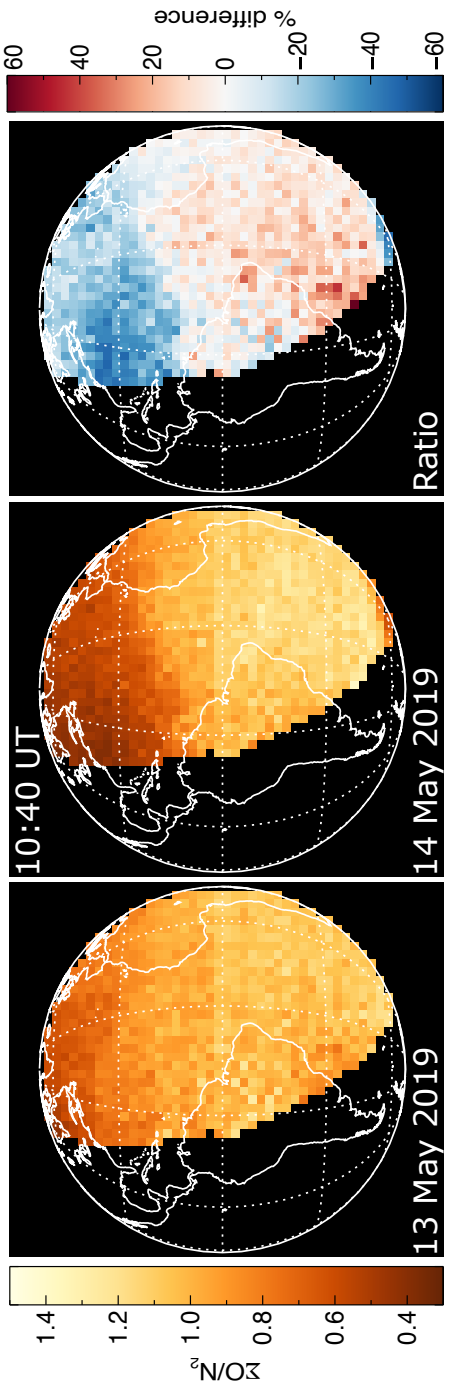

Figure 4. Sample of GOLD Level 2 ON2 data. The north and south hemisphere scans beginning at 10:40 UT for day of year 133 and 134 of 2019 are shownin the left and middle panels, respectively. The right panel shows the percent change from DOY 133 to 134. Note that each image presents two consecutive scans and the mean value is shown for the region where the scans overlap near the equator.

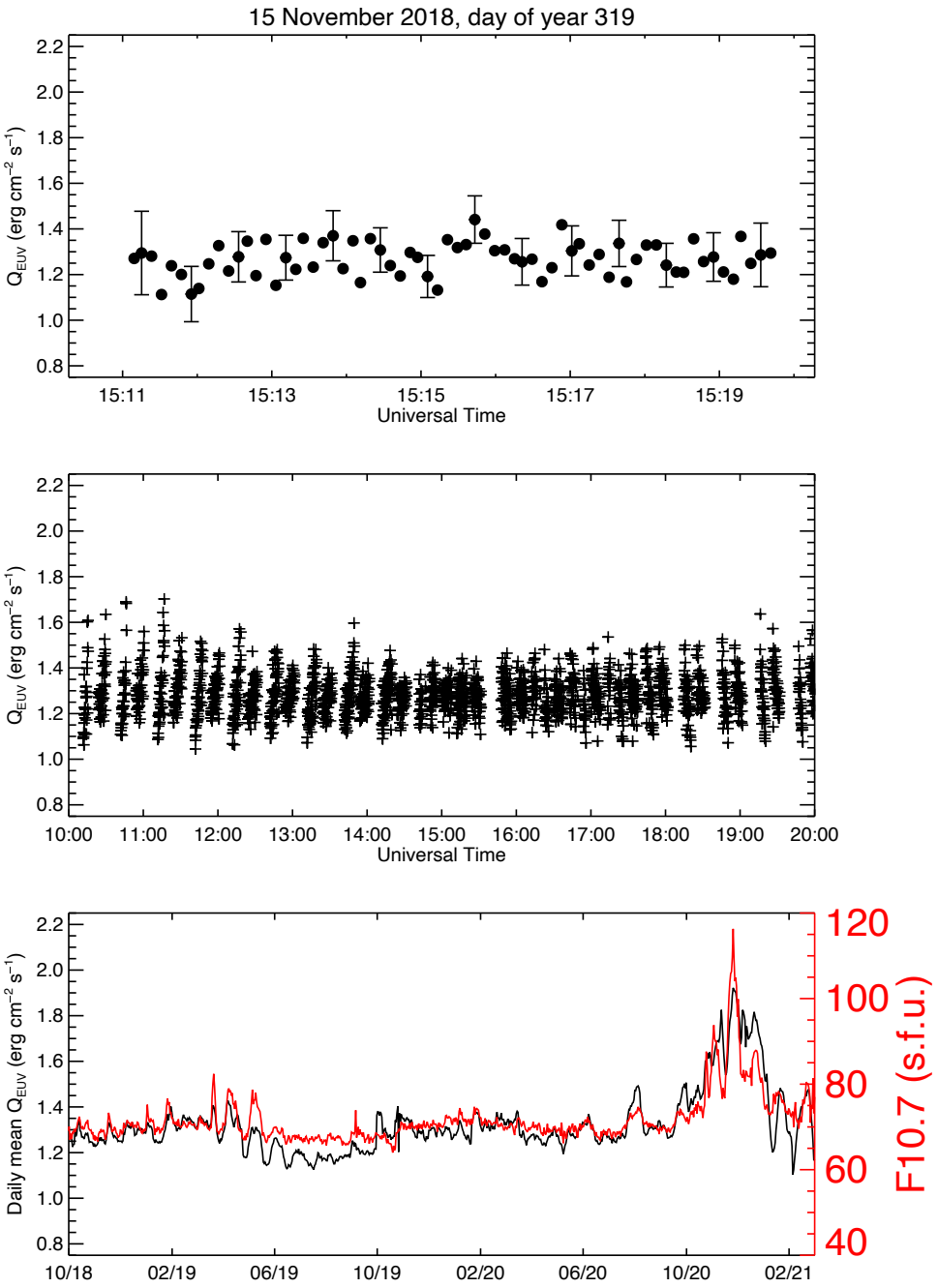

Figure 5. QEUV shown over different time scales. The upper panel shows the variation over the course of a single scan with representative error bars, while the middle panel shows all values from an entire day. The lower panel shows the daily average Q_{EUV} and observed F10.7 over the first two years of the GOLD mission.

Supporting Information for "Thermospheric Composition and Solar EUV Flux from the Global-scale Observations of the Limb and Disk (GOLD) mission"

J. Correira[1], J. D. Lumpe[2], J. S. Evans[1], A. Krywonos[3], R. Daniell[4], V. Veibell[1], W. E. McClintock[5], and R. W. Eastes[5]

[1]Computational Physics, Inc., Springfield, Virginia, USA

[2]Computational Physics, Inc., Boulder, CO, USA

[3]Florida Space Institute, University of Central Florida, Orlando, Florida, USA

[4]Ionospheric Physics Consulting, Stoughton, MA, USA

[5]Laboratory for Atmospheric and Space Physics, University of Colorado, Boulder, Colorado, USA

Contents of this file

Additional Supporting Information (Files uploaded separately)

Introduction

The supporting information consists of additional details on the derivation of ON2, a description of how the error due to radiative recombination was estimated and associated figures, and a movie showing a sequence of 3 days of GOLD Level 2 ON2 data.

Corresponding author: John Correira, correira@cpi.com

Text S1. Detailed Derivation of ON2 Algorithm

In general, the vertical intensity, I_s, (where s =135.6 nm or LBH) of optically thick emissions can be written as

$$I_s(\mu) = \frac{10^{-6}}{4\pi\mu} \int j_s(z) T_s(z,\mu) e^{-\tau(z)/\mu} dz \tag{S.1}$$

where

μ is the cosine of the emission angle (0° for nadir)

$j_s(z)$ is the volume emission rate (photons cm^{-3} s^{-1})

$T_s(z)$ is the self absorption transmission function

$\tau(z)$ is the O_2 pure absorption optical depth

10^{-6} is a conversion factor to unit of Rayleighs

The effect of pure absorption by O_2 is relatively weak for both 135.6 nm and LBH when viewing the Earth's disk. There is a 20% self-absorption effect for the (6,0) N_2 LBH band at 127.3 nm, but it is not included in the bandpass used for ON2 (Conway, 1982). Self-absorption is weak for 135.6 nm (10-15%). While these effects are included in the forward model runs used to construct lookup tables, for the purposes of this discussion it is sufficient to assume $T(z) = e^{-\tau} = 1$. Equation S.1 then reduces to

$$I_s(\mu) = \frac{10^{-6}}{4\pi\mu} \int j_s(z) dz \tag{S.2}$$

The volume emission rate $j_s(z)$ for a given species s is the product of the number density of that species and the emission rate, or g-factor (photons s^{-1}), for the emission of interest

$$j_s(z) = n_s(z) g_s(z) \tag{S.3}$$

yielding

$$I_s(\mu) = \frac{10^{-6}}{4\pi\mu} \int n_s(z) g_s(z) dz \tag{S.4}$$

As with many radiative transfer problems, it is more natural to cast the equations in terms of column densities (or optical depth). The relationship between the total number density n_T and total vertical column density N_T is given by

$$N_T = \int n_T(z)dz \tag{S.5}$$

$$dN_T = n_T(z)dz \tag{S.6}$$

where nadir viewing geometry implies that the integral is over all altitudes. We can use the mixing ratio $f_s = n_s/n_T$ with Equation S.6 and insert into Equation S.4 to recast the problem in terms of total column density

$$I_s(\mu) = \frac{10^{-6}}{4\pi\mu} \int f_s(N_T) g_s(N_T) dN_T \tag{S.7}$$

Making the equation explicit in terms of the ratio of emissions of interest

$$\frac{I_{135.6}}{I_{LBH}} = \frac{\int_{N_{T0}}^{0} f_O(N_T) g_{135.6}(N_T)\, dN_T}{\int_{N_{T0}}^{0} f_{N_2}(N_T) g_{\mathrm{LBH}}(N_T)\, dN_T} \tag{S.8}$$

The vertical column density N_s for a single species may be written in a similar fashion to Equation S.5

$$N_s = \int n_s(z)dz \tag{S.9}$$

Using the mixing ratio and again casting in terms of total column yields

$$N_s = \int f_s(N_T)\, dN_T \tag{S.10}$$

The column density ratio can then be written as

$$\Sigma\mathrm{O}/\mathrm{N}_2 = \frac{N_O}{N_{N_2}} = \frac{\int f_O(N_T) dN_T}{\int f_{N_2}(N_T) dN_T} \tag{S.11}$$

Equations S.8 and S.11 differ only by the presence of the g-factors in Equation S.8, which act as weighting factors on the mixing ratios.

Text S2. Estimate of contribution of Radiative Recombination to Measured O I 135.6 nm

The magnitude of $O^+ + e^-$ radiative recombination (RR) producing 135.6 nm emission is determined by the height integration of the volume emission rate

$$j_{RR}(z) = \alpha_{1356}(z) n_{O^+}(z) n_e(z) \tag{S.12}$$

where α_{1356} is the partial rate coefficient for producing OI 135.6 nm radiation from radiative recombination (Hanson, 1969). The recombination rate's altitude dependence comes from its dependence on the electron temperature. Since the bulk of the emission comes from the F-region of the ionosphere where the dominant ion is singly ionized atomic oxygen, it is reasonable to assume $n_{O^+}(z) \approx n_e(z)$, so that

$$I_{RR} \approx 10^{-6} \int_0^\infty \alpha_{1356}(z)\, n_e^2(z) dz \tag{S.13}$$

yields the approximate column radiance in Rayleighs. A reasonable approximation to the electron density profile (EDP) is a Chapman layer:

$$n_e(z) = n_{\mathrm{e,max}} \exp\left\{\frac{1}{2}\left[1 - \frac{z - z_{max}}{H} - \exp\left(-\frac{z - z_{max}}{H}\right)\sec\chi\right]\right\} \tag{S.14}$$

which can be derived from a simple photochemical model of the F-layer (Schunk and Nagy, 2009). Here, $n_{\mathrm{e,max}}$ is the peak electron density, z_{max} is the altitude of the peak electron density, H is the scale height of the atomic oxygen, from which the ion and electron densities arise, and χ is the solar zenith angle. This is valid for midlatitudes where the geomagnetic field has a large vertical component. At low latitudes, where the geomagnetic field is more nearly horizontal, the ionosphere is more dynamic, and it is not obvious that the scale height should have anything to do with the neutral atmosphere. However, using a number of EDPs measured at the Jicamarca Radio Observatory (located on the geomagnetic equator near 70^o W longitude) we have found that this profile shape (with $\chi = 0^o$) can be fit to the EDP in the F-region using H as a free parameter. At least for solar minimum conditions, H takes on values near 50 km, which is approximately the scale height of atomic oxygen.

Substituting S.14 into S.13 while neglecting the altitude dependence of α_{1356} and making reasonable approximations with the integration limits, results in an expression for I_{RR}:

$$I_{RR} \approx 10^{-6} \alpha_{1356} n_{e,\mathrm{max}}^2 H e \tag{S.15}$$

where e is the base of natural logarithms, not the elementary charge. If α_{1356} is in cm^3 s^{-1}, $n_{\mathrm{e,max}}$ is in cm^{-3} and H is in cm, I_{RR} will be in Rayleighs. While useful in some circumstances, this expression requires the knowledge of the peak electron density, which is not available everywhere at all times. Using S.14, one can also derive an expression for the TEC:

$$TEC \approx 10^{-12} n_{\mathrm{e,max}}\ H\sqrt{2\pi e} \tag{S.16}$$

If $n_{\mathrm{e,max}}$ is in cm^{-3} and H is in cm, TEC will be given in TECu (= 10^{12} cm^{-2}). From this we may obtain

$$n_{\mathrm{e,max}} \approx \frac{10^{12}\mathrm{TEC}}{H\sqrt{2\pi e}} \tag{S.17}$$

Finally, substituting S.17 into S.15 produces an expression relating the column brightness of OI 135.6 nm emission to TEC:

$$I_{RR} \approx 10^{18} \frac{\alpha_{1356}}{2\pi H} (TEC)^2 \tag{S.18}$$

If TEC is in TECu, H is in cm, and α_{1356} is in cm^3 s^{-1}, then I_{RR} will be in Rayleighs. A good value for the recombination rate is $\alpha_{1356} = 7.3 \times 10^{-13}(1160/T_e)^{0.7}$ cm^3 s^{-1} [Meléndez-Alvira et al., 1999; Tinsley et al., 1973]. Note that there are many approximations used in deriving this expression, not the least of which is that a Chapman layer provides a good description of the complete EDP, and we ignore the fact that GPS derived TEC includes the topside and plasmasphere contributions, which will bias the derived $n_{\mathrm{e,max}}$ values (and the resulting OI 135.6 nm radiances) to higher values.

While a full exposition of 135.6 nm emission from RR over the range of possible spatial and temporal variations is beyond the scope of this technical report, average values can provide a sense of the magnitude of the contribution to the 135.6 nm signal measured by GOLD. All vertically integrated electron density data from 2019 (obtained from the CEDAR Madrigal Database, Anthea Coster, MIT/Haystack Observatory, http://cedar.openmadrigal.org/) was converted to magnetic coordinates and binned by magnetic latitude, longitude, and solar local time. The binned TEC was then averaged across magnetic longitude and converted to 135.6 nm emission using Equation S.18, yielding a map of mean 135.6 nm intensity as a function of magnetic latitude and solar local time. The binned TEC can be seen in Figure S1, while Figure S2 shows the resulting 135.6 nm intensities. Figure S2 demonstrates both the spatial extent and diurnal evolution of the EIA can clearly be seen in 135.6 nm emission. Line plots in the bottom and right hand panels correspond to the horizontal and vertical dashed yellow lines, respectively. The bottom panel shows the

diurnal evolution of the 135.6 nm RR source at -15° magnetic latitude, while the right hand panel shows the two crests and latitudinal extend of the emission at 14:00 local time. The mean magnitude of the 135.6 nm intensity from RR for very low geomagnetic activity is on the order of 10 Rayleighs.

Figure S3 shows the median 135.6 nm radiance derived from GOLD data as a function of solar zenith angle and emission angle for data from 2020 (through September). All data are gathered into bins 1° in solar zenith angle by 1° in emission angle and the median value is calculated. The magnitude varies with solar illumination (and geophysical conditions which are averaged together here) but are typically at least several hundred Rayleighs. Therefore any error due to the inclusion of 135.6 nm emission from RR is small for the low geomagnetic activity conditions observed by GOLD to date. As can be seen in Figure 2 the relationship between the 135.6/LBH intensity ratio and $\Sigma O/N_2$ is nearly linear for small changes in the intensity ratio. For example, a measured 135.6 nm signal that contains a 5% RR component results in a derived $\Sigma O/N_2$ that is ∼5% too large. Should the RR contribution become more significant during periods of increased solar and geomagnetic activity, the error in $\Sigma O/N_2$ attributable to inclusion of 135.6 nm from RR can be estimated using this relationship.

O I 135.6 nm brightness is also an input for the Q_{EUV} algorithm both directly and indirectly through $\Sigma O/N_2$. In the case of RR contamination the increase in both the 135.6 nm brightness and $\Sigma O/N_2$ tend to offset one another when computing Q_{EUV} (discussed below). In the context of GOLD QEUV, RR contamination is further mitigated by using only midlatitude spatial pixels away from the EIA to minimize 135.6 nm contributions from RR.

The foregoing qualitative arguments can also be demonstrated quantitatively by using simulated radiances with and without RR contamination as input to the ON2 and QEUV algorithms. For this example, the true O I 135.6 nm and N_2 LBH radiances are 1000 R and 475 R, respectively. 135.6 nm RR contributions of 10, 50, and 100 R were added to the true radiance for a range of solar zenith angles from 0 to 70 degrees. The resulting contaminated $\Sigma O/N_2$ values were larger than the true value by nearly the same amount as the RR fractional contribution to the total 135.6 nm intensity (i.e. 1, 5, and 10%) and varied little with solar zenith angle. On the other hand, the simulated Q_{EUV}

with RR contamination was no more than ∼3% larger than the true Q_{EUV} for even the 10% RR contamination case.

It is important to emphasize that a similar analysis should be undertaken by users of GOLD ON2 data for the locations, local times, geomagnetic and solar activity conditions appropriate for their study. The use of 2019 TEC data only provides a lower bound on the 135.6 nm RR contribution due to the quiet solar and geomagnetic conditions, and as activity increases during Solar Cycle 25 the RR contribution to measured 135.6 nm will increase. During more active solar conditions TEC values of ∼100 occur during midday (e.g. Romero-Hernandez et al., 2018), which implies a ∼230 Rayleigh contribution from RR, resulting in a 20% or larger error in $\Sigma O/N_2$.

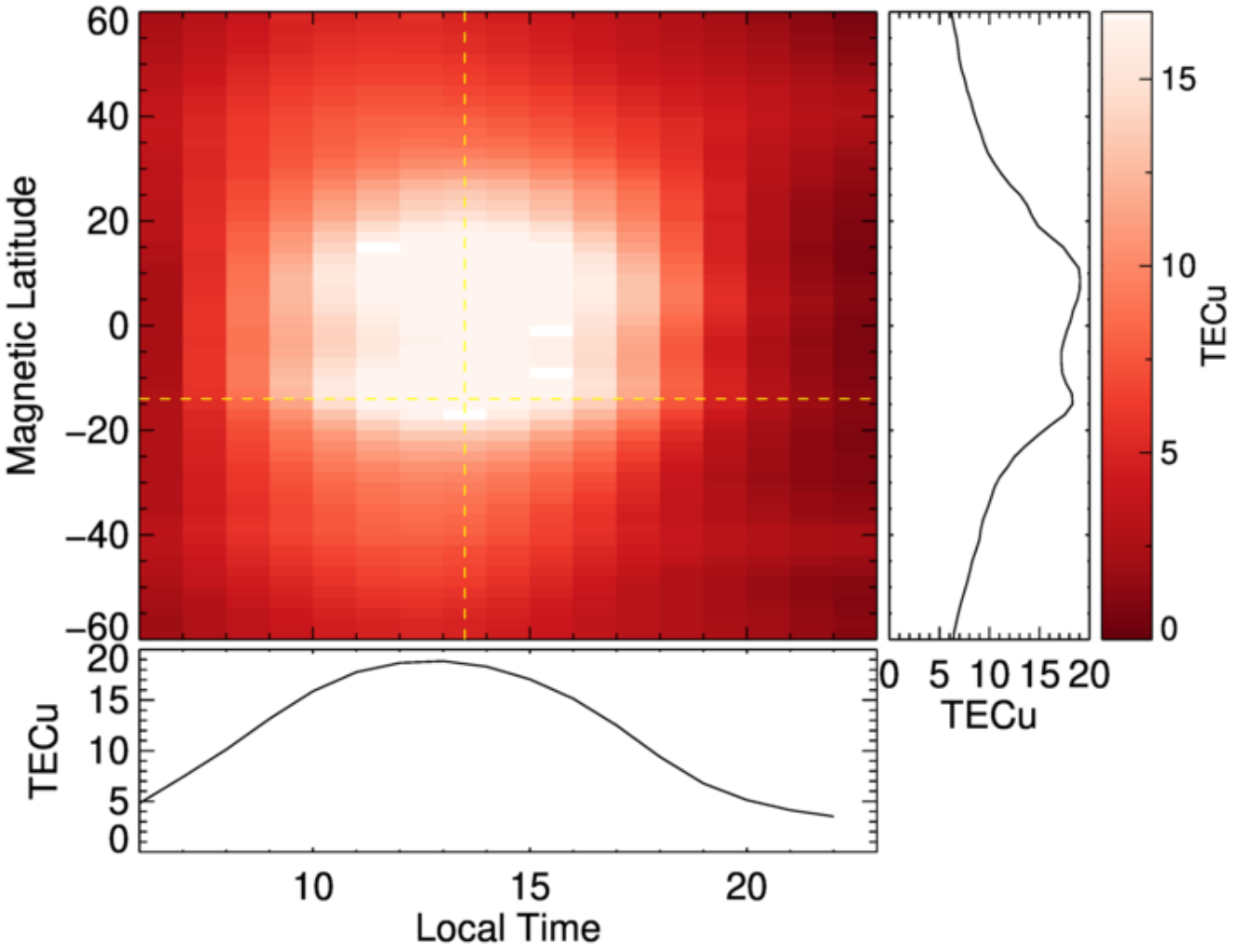

Figure S1. Vertical total electron content derived from GPS data as a function of magnetic latitude and local time averaged across all magnetic longitudes. Horizontal and vertical dashed yellow lines indicate the location of the local time and latitude profiles shown in the bottom and right hand panels, respectively.

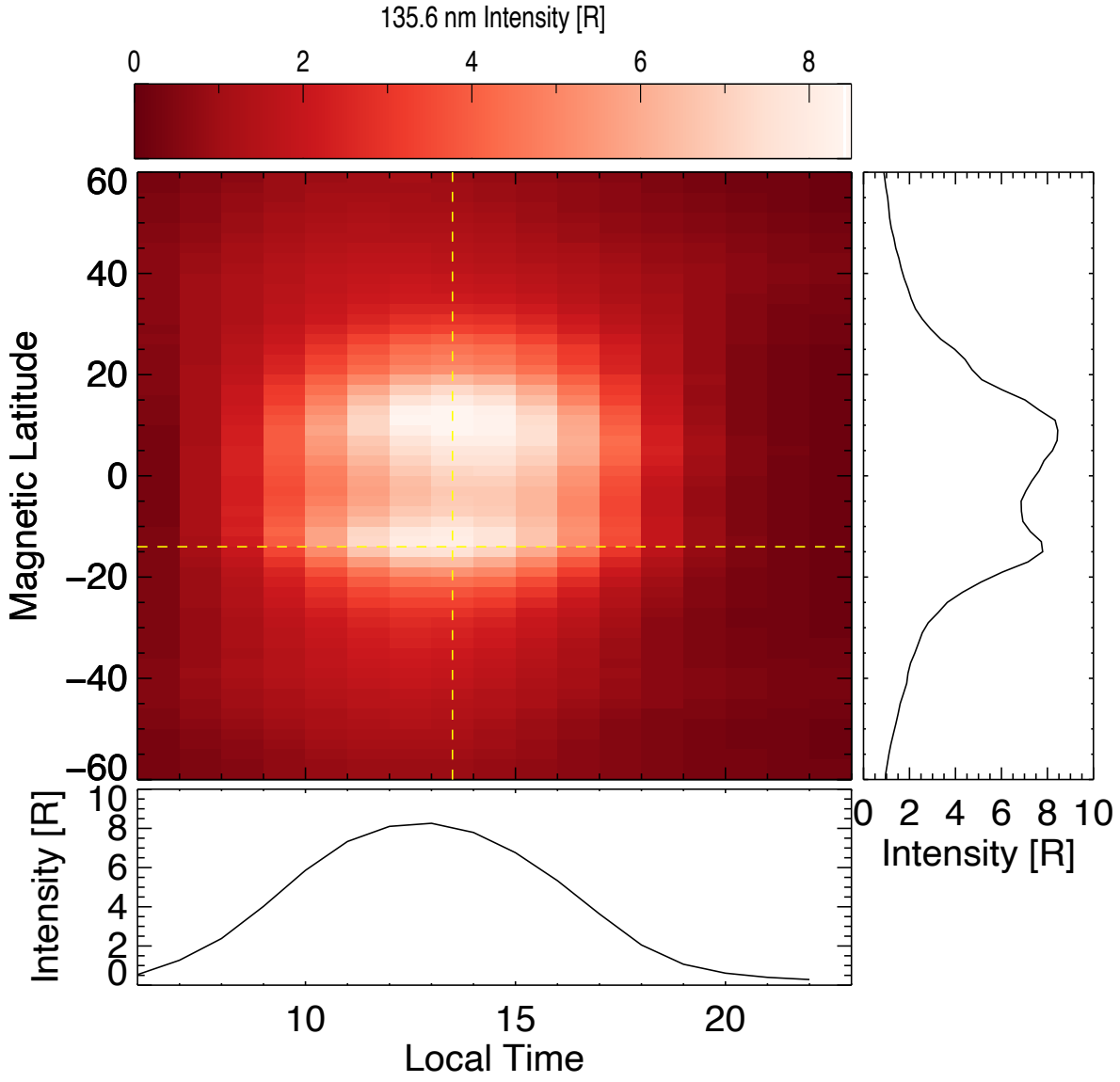

Figure S2. 135.6 nm intensity due to radiative recombination derived from TEC (shown in Figure S1 as a function of magnetic latitude and local time averaged across all magnetic longitudes. Horizontal and vertical dashed yellow lines indicate the location of the local time and latitude profiles shown in the bottom and right hand panels, respectively.

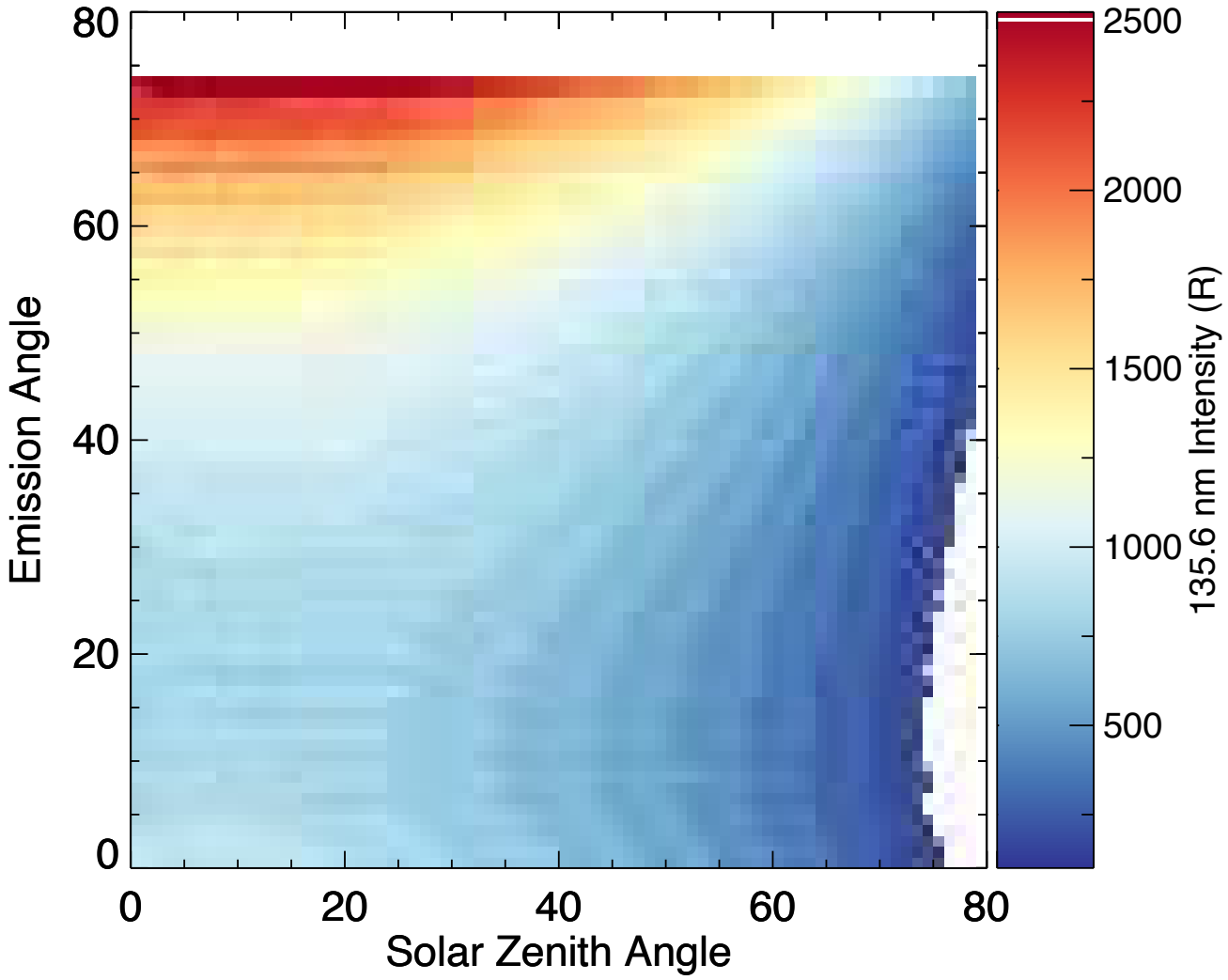

Figure S3. Median 135.6 nm intensity measured by GOLD in bins 1° in solar zenith angle by 1° in emission angle.

Movie S1.

The file 2021JA029517-ms01.mp4 shows three days of GOLD Level 2 ON2 data from 13 May 2019 to 15 May 2019. It shows the day before, day of, and day after the May 2019 storm (images shown in paper). In addition to demonstrating storm effects it is also a representative example of GOLD ON2 data. Note that each image presents data from two consecutive scans (i.e. a northern hemisphere scan and southern hemisphere scan) and the mean value is shown for the region where the scans overlap near the equator. Times shown indicate the start time of the northern hemisphere scan. The southern hemisphere scan starts 12 minutes after the northern hemisphere.